The Astrophysical Journal, 893:87 (13pp), 2020 April 20 https://doi.org/10.3847/1538-4357/ab8292

Satellite Alignment. III. Satellite Galaxies' Spatial Distribution and Their Dependence on Redshift with a Novel Galaxy Finder

Lin Tang (唐林), Weipeng Lin (林伟 鹏), and Yang Wang (汪洋)
School of Physics and Astronomy, Sun Yat-sen University, DaXue Road 2, 519082, Zhuhai, People's Republic of China; tanglin23@mail.sysu.edu.cn, linweip5@mail.sysu.edu.cn
Received 2019 December 6; revised 2020 March 20; accepted 2020 March 22; published 2020 April 20

Abstract

After being extensively explored, observations and theories have shown that satellites are preferentially aligned with major axes of their host centrals. There are still some unresolved issues on this topic. In this paper, we present studies on satellite spatial distribution. To fairly compare with observations, we develop a novel galaxy finder and reconstruction algorithm in hydrodynamical simulation, which is based on the projected mock image, taking into account the full consideration of the point-spread function, pixel size, surface brightness limit, resolution, and redshift dimming effects. With galaxy samples constructed using such an algorithm, the satellite alignment is examined by comparing with observational results. It is found that the observational alignment can be reproduced for red galaxies, which dominate the sample in this study, but not for blue galaxies. Satellites' radial distribution is also investigated. It exhibits that outer satellites within host halos show stronger alignment signal than satellites in the inner regions, especially for red satellites, which is in contrast with previous studies. The disagreement is mainly due to extra galaxies identified by our new galaxy finder, which are mainly located in the inner region of host halos. Our study illustrates that at lower redshift, the alignment strength becomes stronger, while the radial distribution curve becomes flatter. This suggests differences in the evolution of the angular distribution between satellites residing in the inner and outer halos and implies that the post-infall evolution reduces the original alignment signal and that the impact decreases for satellites with later infall times.

Unified Astronomy Thesaurus concepts: Galaxy formation (595); Galaxy structure (622); Computational methods (1965); Observational astronomy (1145); Astrostatistics (1882)

1. Introduction

Modern observational results suggest the formation of cosmic structure as hierarchical clustering, where small halos form first and subsequently merge to form bigger ones. Although current cosmology based on a ΛCDM model is successful in explaining large cosmic structure (e.g., Bahcall et al. 1999), a lot of research works have found that there are some serious discrepancies between observations and simulations, such as the core–cusp problem, missing baryons, too-big-too-fail problems, etc. (e.g., Klypin et al. 1999; Maller & Bullock 2004; Boylan-Kolchin et al. 2011; Walker & Peñarrubia 2011). Those tensions mainly occur on small scales, where the structure formation is dominated by nonlinear astrophysical processes (e.g., Bertschinger 1998; Dolag et al. 2008; Kuhlen et al. 2012). The aforementioned problem can be partly solved by the modified baryonic model in galaxy formation (e.g., Bullock & Boylan-Kolchin 2017). The spatial distribution of satellite galaxies is one of the most important characteristics of small-scale structure, which is associated with the galaxy dynamics and mass distribution (e.g., Knebe et al. 2004; Sales et al. 2007). Accurate prediction on satellite spatial distribution can provide important clues for structure formation on small scales and may help to solve the tension in some degree.

The study on satellite spatial distribution has a long history. There were no converged conclusions in early observational studies. For example, Holmberg (1969) studied the satellites of local galaxies and found that the satellite galaxies distribute peculiarly to the disk of central galaxies. In other words, most of them align along the minor axis of central galaxy, named the Holmberg effect. However, Sastry (1968) found that there is a strong tendency for the distribution of galaxies to be oriented along the major axes of the cD galaxies (centrals of clusters). Benefited by the development of large galaxy surveys, such as the 2dF Galaxy Redshift Survey, observations have manifested statistical evidence of the Holmberg effect (Sales & Lambas 2004), but only for a very specific subsample with radial velocity relative to the primary $|\Delta v| < 160$ km s^{-1}.

With a more complete sample and no specific selection criteria, the Sloan Digital Sky Survey (SDSS) has shown that the satellites are preferentially distributed along the major axes of centrals (Yang et al. 2006, hereafter Y06). Y06 used the galaxy group catalog of Weinmann et al. (2006), which is constructed based on the New York University Value-Added Galaxy Catalogue (Blanton et al. 2005), with the galaxy group finder developed by Yang et al. (2005). This group finder links galaxies into groups by the friends-of-friends (FoF) algorithm (Davis et al. 1985). Then, it estimates the host halo mass and viral radius according to the group member galaxies and kicks off galaxies out of viral radius. This process is repeated iteratively until the galaxy group catalog converges. In each galaxy group, the brightest member is treated as the central galaxy, while other members are treated as satellite galaxies. In addition, Y06 compared with previous studies and found that the inconsistency is mainly caused by the small sample size and misinterpretation of the position angle. The phenomenon in Y06 is widely confirmed by subsequent investigations (e.g., Faltenbacher et al. 2007; Bailin et al. 2008; Agustsson & Brainerd 2010).

The previous observational studies have investigated that the strength of satellite alignment depends on the galaxy properties, such as color of centrals and satellites (e.g., Azzaro et al. 2007), radius between the centrals (e.g., Brainerd 2005;

Brainerd & Yamamoto 2019), and surrounding environment (e.g., Zhang et al. 2015; Wang et al. 2018). The relationship between satellites' spatial distribution and galaxy properties indicates that satellite alignment is connected with galaxy formation and evolution and can be a tracer of the small-scale cosmic structure. Many theoretical works have claimed that satellite alignment can be reproduced in a cold dark matter (CDM) model and interpreted by the nonspherical nature of dark matter halos, in which satellites are aligned with the major axes of host centrals (e.g., Kang et al. 2005b; Agustsson & Brainerd 2010; Wang et al. 2014b).

However, the main discrepancy between observational and theoretical studies is that the alignment strength of observations is commonly weaker than the prediction of simulations (e.g., Kang et al. 2007; Faltenbacher et al. 2008; Bett et al. 2010; Bahl & Baumgardt 2014) and the dependence on galaxy properties is poorly reproduced (e.g., Agustsson & Brainerd 2010).

Many works attempted to solve those problems. Kang et al. (2007) studied the galaxy alignment using an *N*-body simulation that includes a semianalytical model for galaxy formation and compared the results with those in Y06. They stated that the galaxy catalog in Y06 is impacted by the interlopers (i.e., nearby galaxies identified as satellites by the galaxy finder). Furthermore, they argued that the galaxy catalog is significantly incomplete, caused by two main selection effects: the observational apparent magnitude limit of $m_r < 22.2$ mag for galaxies, and the group finder criterion of $M > 10^{12}\,h^{-1}\,M_{\odot}$ for their host halos. Those effects reduce the galaxy alignment signal and produce an artificial dependence of alignment strength on the color of the central galaxy. Wang et al. (2014b, hereafter Paper I) used an *N*-body simulation to explore overprediction of satellite alignment and its dependence on the mass, formation time of host halos, and accretion time of subhalos. The central galaxy shares the same shape as the inner region of host halos, and subhalos are used to trace the positions of satellite galaxies. This work can reproduce the satellites' spatial distribution (represented by the probability function of distribution angles) using the inner halo shape but shows no dependence of alignment on the color of satellites caused by the limitation of pure *N*-body simulations. Dong et al. (2014, hereafter D14) reproduced the observational alignment signal and the color dependence well utilizing a hydrodynamical cosmological simulation. They also found that satellite alignment depends strongly on satellite metallicity. But the color dependence has a low confidence level caused by a lack of active galactic nucleus (AGN) feedback in simulation.

Brainerd & Yamamoto (2019) investigated the locations of luminous satellite galaxies using the hydrodynamical simulation Illustris, which includes a complete galaxy formation model, and found that the misalignment between mass and luminosity can affect the anisotropy of the satellite distribution. Moreover, they found that the anisotropy of the satellite distribution decreases with three-dimensional distance between satellites and hosts, which is completely in contrast with previous studies (e.g., Yang et al. 2006; Dong et al. 2014; Wang et al. 2018).

Moreover, the redshift evolution of galaxy alignment has been poorly studied. Donoso et al. (2006) used the SDSS DR4 to study the alignment of luminous red galaxies at $z \sim 0.5$. The result is similar to that in the local universe. Wang et al. (2010) created a high-redshift ($0.4 < z < 1.0$) group catalog out of a spectroscopic sample of galaxies in the GOODS fields and studied the distribution of satellite galaxies. They found that there is no significant difference between the alignment strength in high-z and local groups for the total samples, but the generality of this conclusion could have been limited by the small sample size. In their discussion, they argue that a weaker alignment signal is expected at higher redshifts. Samuroff et al. (2020) tested the satellite anisotropy using the MassiveBlack-II simulation, and it was found that there is no evidence of coherent evolution for galaxy intrinsic alignment with redshift, but with large scatter in small scales.

The galaxy is usually defined as a group of bounding particles in simulations. Apparently, it is very different to define bounding groups in observations where surface brightness is in consideration. Therefore, when making comparisons, inconsistency in methods will influence the analysis of difference between simulation results and observations and eventually reduce the reliability of conclusions. In a previous paper (Tang et al. 2018), we argued that the general trend of intracluster light (ICL) redshift evolution in observational results agrees with our theoretical predictions, using the mocking projected image and similar observational parameters in simulation. We emphasize the importance of using the same definition when observational results are compared with theoretical predictions.

In this paper, we will reexamine the satellite spatial distribution and its dependence on redshifts, using a novel method that mimics observation. We develop a novel galaxy finder and reconstruction algorithm in hydrodynamical simulation, which is based on the projected mock image modified with a point-spread function (PSF), pixel size, surface brightness limit, resolution, and redshift dimming effects. In such a way, the comparison between observations and theories will be much fairer than previous studies.

The paper is organized as follows. In Section 2, we briefly describe the simulation we used, how we determine the mock galaxies, and the galaxy sample with a set of selection criteria. In Section 3, we show the satellites' spatial distribution, including the results of alignment signal, dependence on radii of dark matter halos, and redshifts. We summarize and briefly discuss our results in Section 4.

2. Methodology

2.1. Simulation

The cosmological simulation was run with the GADGET-2 code (Springel 2005), which is the same simulation used in previous works (Dong et al. 2014; Tang et al. 2018). It runs in a ΛCDM universe, with $\Omega_m = 0.268$, $\Omega_\Lambda = 0.732$, $\sigma_8 = 0.85$, $h = 0.71$, and 512^3 DM and 512^3 gas particles in a cubic box with a side length of $100\,h^{-1}$ Mpc. The Plummer softening length is 4.5 kpc, and each dark matter and gas particle has a mass of $4.62 \times 10^8\,h^{-1}\,M_{\odot}$ and $9.20 \times 10^7\,h^{-1}\,M_{\odot}$. The gas particle can be turned into two star particles later on. The simulation includes gas cooling, star formation, and SN feedback, but no AGN feedback. Dark matter halos are defined by the FoF algorithm with a linking length of 0.2 times the mean particle separation. Each star particle of the FoF group is treated as a simple stellar population with age, metallicity, and mass given by the corresponding particle's properties in the simulation. The FoF algorithm agrees remarkably well on fundamental properties of dark matter halos, compared with other halo finders using high-resolution cosmological simulations (e.g.,

Knebe et al. 2011). Only halos with a minimum particle number of 60 will be selected for later analysis. Readers interested in detailed description of the simulation are referred to Springel & Hernquist (2003) and Lin et al. (2006).

2.2. Mock Observation of Galaxy

Although lacking AGN feedback causes an overcooling problem, producing bluer central galaxies as shown in D14, our method looks realistic, and the discrepancy of fraction and evolution of ICL between observations and predictions could be partly reduced (Tang et al. 2018). Stellar magnitude is calculated using the simple stellar population model of Bruzual & Charlot (2003, hereafter BC03). The calculation of surface brightness and projection method has been described in Tang et al. (2018). We only introduce the definition of the mock galaxy here.

First, given a PSF width ω and a CCD pixel size α, we obtain the projection image of each FoF group in three different planes, $x-y$, $y-z$, $z-x$. A surface brightness profile brighter than 30 mag arcsec^{-2} in V band is applied. Then, applying a given magnitude limit (or surface brightness limit, SBL) in V band, we get the luminosity part above the SBL as galaxy components. Finally, we define grids connected together as one galaxy using a scheme similar to the FoF group finder. Galaxy properties, such as mass, age, color, and metallicity, are calculated by the light-weighted method. Particularly, the galaxy shape is defined by the ellipse fitting of all galaxy components. The major axis is computed by the density profile, which is similar to the method by the surface brightness isophote in previous observational studies.

Color $(g-r)$ is defined by BC03 magnitude in SDSS g band minus that in SDSS r band. Considering the comparison between different redshifts, we shift $(g-r)$ to color at $z=0.1$, $^{0.1}(g-r)$ using $^{0.1}(g-r) = 0.7088 - 1.3197[(g-r) - 0.6102]$ (Blanton & Roweis 2007). Yang et al. (2006) simply adopted $^{0.1}(g-r) = 0.83$ to divide galaxies into red and blue subsamples, without taking into account the dependence of color on galaxy stellar mass or magnitude. This method is too simple and results in some red galaxies being assigned as blue galaxies. As we discussed in Section 3.2, red and blue galaxies show a different spatial distribution. In fact, it is more reasonable that the division between red and blue galaxies is stellar mass dependent (e.g., van den Bosch et al. 2008). Therefore, we divide the galaxies into reds and blues using the fitting line of van den Bosch et al. (2008).

We test the impacts of ω and α in galaxy definition and find that smaller ω and pixel size α make the projection image more similar to the original image of groups. Considering the spatial resolution in our simulation, we chose the Plummer softening length as the physical distance of ω and α for each redshift. In addition, as stated in Tang et al. (2018), the PSF and pixel size effects are more significant for diffuse or underdense regions. By applying the selection criteria in the next section, the diffuse stellar components should have been removed to ensure clear galaxy boundary.

It is found that galaxy number and physical properties vary significantly in the projected image with different SBLs. As shown in Figure 1, we simply explore the surface brightness profile of the brightest galaxy at $z\sim 0$ with five different SBLs, [24.7, 26.5, 28, 29, 30] mag arcsec^{-2} at V band. Table 1 simply shows the physical properties of the brightest central galaxy defined by different SBLs. Figure 1 shows that the surface brightness profiles of the brightest central galaxy are obviously varied with SBLs. It is found that the profiles have fluctuations at large galactocentric radii for the faintest SBLs, due to the contamination from satellites. And the profile with the brightest SBL (24.7 mag arcsec^{-2}) shows a too small radius, which only includes the central part. To avoid these problems, we define galaxies by a reconstruction procedure with multiple SBLs (e.g., 24 − 30 mag arcsec^{-2}). The final galaxy sample is obtained by combining the results from different SBLs.

The reconstruction procedure includes the following steps:

1. We define the mock galaxies by a series of SBLs (e.g., [30, 27, 24] mag arcsec^{-2} with a bin width of 3).
2. We compare the mock galaxies defined by two SBLs, for example, [30, 27] mag arcsec^{-2}. Those galaxies defined by the faint SBL (30 mag arcsec^{-2}), but not shown in the sample defined by the bright SBL (27 mag arcsec^{-2}), will be included in a temporary sample of reconstructed galaxies.
3. Mock galaxies simultaneously defined by the two SBLs will be also included in the temporary sample. Each galaxy in this sample will be checked whether it can be separated into several galaxies or not with the bright SBL. If not, the target galaxy defined by the faint SBL will hold its position in the sample. Otherwise, the target galaxy will be excluded from the sample and the separated galaxies defined by the bright SBL will be included in the sample.
4. We use this galaxy sample to make the comparison with the one defined by a brighter SBL (repeating second and third steps) and obtain the final sample of reconstructed galaxies.

An example of the reconstruction procedure is illustrated by Figure 2, in particular to show how it works for the second and third steps. It is found that different galaxies are defined by three different SBLs. A complete galaxy catalog in the right panel of Figure 2 is set up by the above reconstruction procedure, compared with the initial state of only one big distinct galaxy and one faint galaxy shown in the left panel of Figure 2 (not for the real dark matter halo).

We apply an SBL width equal to 0.5 for an SBL range from 24 to 30 mag arcsec^{-2} in the reconstruction procedure. Figure 3 illustrates the galaxies with each SBL and the final reconstructed galaxies in the central region of the most massive dark matter halo. It should be noted that the final reconstructed sample has components with vary small radius or low mass, which should not be trusted as galaxies. This will be discussed in the next section. The last row of Table 1 simply shows the physical properties of the brightest galaxy defined by the reconstruction procedure. The surface brightness profile of the reconstructed brightest galaxy is shown in Figure 4. It is apparent that the problems (fluctuations and small radius) caused by the usage of a single SBL have been avoided, and the surface brightness profile becomes smooth. In general, 26.5 mag arcsec^{-2} is commonly applied to distinguish the galaxy and ICL in observations (e.g., Feldmeier et al. 2004; Presotto et al. 2014). And the galaxy (especially the central brightest galaxy) has a fine surface brightness profile compared with de Vaucouleurs ($R^{1/4}$) or Sersic ($R^{1/n}$) models by using this SBL (e.g., Gonzalez et al. 2005; Zibetti 2008). As shown in Figure 1, there is a feature of fluctuation on the edge region of the central galaxy. After the reconstruction, we can reproduce

Table 1
Properties of the Brightest Galaxy in Simulation for Different Surface Brightness Limits and Reconstruction

$\mu_{V,\rm limit}$	M_*	L	Met	Age	$^{0.1}(g-r)$	Radius
(mag arcsec^{-2})	($10^{12}\,h^{-1}\,M_\odot$)	($10^{12}\,h^{-1}\,L_\odot$)	Log($Z/Z_\odot$)	(Gyr)	(mag)	(h^{-1} kpc)
24.7[a]	4.80	1.16	−1.81	9.89	0.80	30.63
26.5[a]	6.15	1.40	−1.91	9.95	0.81	73.80
28.0[a]	7.63	1.70	−2.05	9.96	0.81	154.90
29.0[a]	9.03	2.01	−2.14	9.75	0.80	245.19
30.0[a]	11.9	2.67	−2.26	8.53	0.79	510.73
26.65[b]	6.32	1.44	−1.93	9.95	0.81	81.94

Notes. The brightest galaxy in simulation is located in the most massive dark matter halo with viral mass $M_{\rm vir} = 6.23 \times 10^{14}\,h^{-1}\,M_\odot$. For a galaxy obtained by the reconstruction procedure, the $\mu_{V,\rm limit} = 26.65$ here is the surface brightness at the galaxy edge. This is different from others.
[a] Brightest galaxy defined by the different surface brightness limits.
[b] Brightest galaxy obtained by the reconstruction procedure with multiple SBLs.

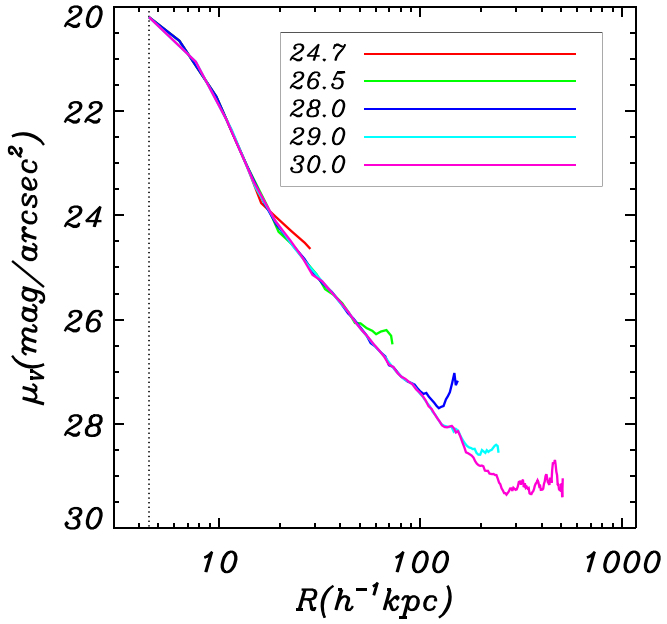

Figure 1. Surface brightness profile of the brightest galaxy in simulation at $z \sim 0$ with five different SBLs, $\mu_{V,\rm limit} = 24.7, 26.5, 28, 29, 30$ mag arcsec^{-2}. The vertical dotted line represents the Plummer softening length in the simulation.

the galaxy size defined by SBL = 26.5 mag arcsec^{-2}, and the galaxy has a flat surface brightness profile that looks similar to a cD galaxy, as shown in Figure 4. As one can see, the impact by neighbor galaxies has been removed. The profile in the outer region is well fitted by $R^{1/4}$ or $R^{1/n}$ models. On the other hand, the bulge is much brighter and its surface brightness profile exceeds the model prediction, caused by the overcooling problem and possible overmerging problem in our simulation.

As stated in Kang et al. (2007) and Wang et al. (2014b), the "orphan" galaxies (i.e., galaxies with unresolved or tidally disrupted small subhalos) are important for the satellite alignment signal. The "orphan" galaxies mostly reside in the inner region of host halos. Those galaxies are commonly included by the main subhalos defined by the substructure finder. Using our reconstruction procedure, these galaxies can be clearly distinguished. It is also worth noting, utilizing state-of-the-art cosmological simulations, that it is found that most disruption (or "orphan galaxy") is numerical in origin (e.g., van den Bosch et al. 2018; van den Bosch & Ogiya 2018). We will come back to this problem using present-day simulations, e.g., the Illustris simulation.

2.3. The Refinement of Galaxy Sample

The Plummer softening length is $\epsilon = 4.5\,h^{-1}$ kpc, and each stellar particle has a mass of $4.62 \times 10^7\,h^{-1}\,M_\odot$ in our simulation. Commonly, substructures with stellar mass and size under a given value, associated with resolution in simulation, are not treated as galaxies.

As shown in the top panel of Figure 5 for the full sample without any selection, the stellar mass function of central galaxies peaks at $M_* \sim 10^9\,h^{-1}\,M_\odot$ and declines sharply toward the lower mass end. Furthermore, for satellite galaxies, it shows unreasonable peaks in $M_* < 10^9\,h^{-1}\,M_\odot$. Considering the computational accuracy of centrals' axis and reliability of galaxies (e.g., Bett et al. 2007; Wang et al. 2015), we set a mass resolution criterion to select only central and satellite galaxies more massive than $9.2 \times 10^9\,h^{-1}\,M_\odot$ and $4.6 \times 10^9\,h^{-1}\,M_\odot$, respectively, which are approximately 200 and 100 times mass resolution, and enough for resolving the structures of galaxies (Bett et al. 2007). Table 2 shows the sample definitions. On the other hand, the criteria are above the peak position of the mass function, which guarantees the completeness of the galaxy sample.

In the bottom panel of Figure 5, we plot the galaxy radius number distribution for the sample with the mass resolution criterion applied. It is found that the galaxy radius distribution peaks at $\sim 15\,h^{-1}$ kpc. With the mass resolution criterion, we set a size criterion to select only galaxies with radii larger than $18\,h^{-1}$ kpc, approximately 4 times the spatial resolution, which is slightly larger than the peak value of the galaxy radius distribution.

The lower limits of radius and particle number for our selected galaxies ($r_h/\epsilon > 4$ and $N > 200$ (100)) are slightly smaller than the criteria in van den Bosch & Ogiya (2018) ($r_h/\epsilon > 6.9$, $N > 250$). But keep in mind that our method is more conservative since it cuts off more particles close to the edges of each galaxy. Thus, these slightly lower criteria will not bring more fake galaxies.

The SBL bin width is associated with the observational magnitude resolution. Considering the two selection criteria above, we reconstruct galaxies with five SBL bin widths, [0.1, 0.2, 0.3, 0.4, 0.5], to investigate the selection effect of SBL bin width. We present the dependence of galaxy number distributions on the faintest surface brightness in the outermost region

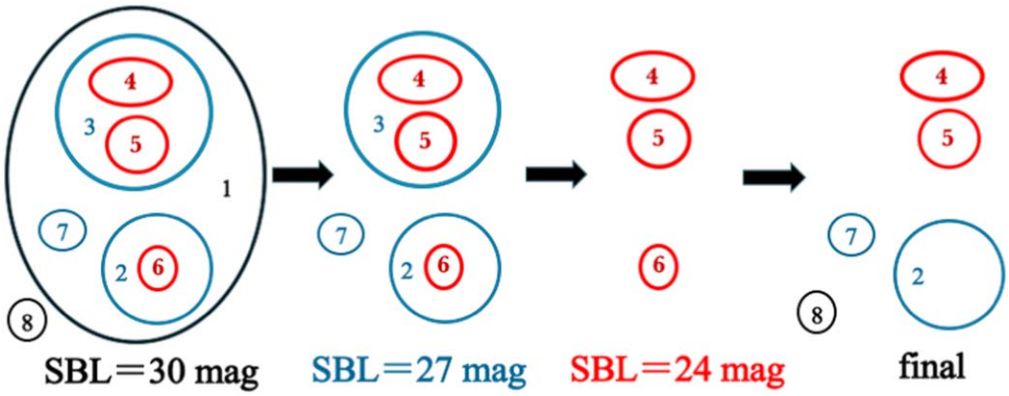

Figure 2. Example for the reconstruction procedure. We choose three SBLs, 30(*black*), 27(*blue*), 24(*red*) mag arcsec^{-2}. The left panel shows the surface brightness profile for the chosen SBLs. It is found that there are only two distinct galaxies, denoted as 1 and 8, for the faintest SBL, 30 mag arcsec^{-2}. With a brighter SBL, 27 mag arcsec^{-2}, the distinct galaxies are denoted as 2, 3, and 7. Galaxy 8 is so faint that it disappears. Galaxy 3 is separated into two galaxies, denoted as 4 and 5; galaxy 7 is so faint that it disappears; and galaxy 2 is altered to galaxy 6, with SBL = 24 mag arcsec^{-2}. Rather than the three galaxies (denoted as 4, 5, and 6) defined by the brightest SBL of 24 mag arcsec^{-2}, we select galaxies denoted as 2, 4, 5, 7, and 8 for the final distinct galaxies by using our reconstruction procedure in this example.

of galaxies, i.e., the lowest value of surface brightness profile of galaxies, which is the mean surface brightness on the edge region of galaxies shown in Figure 6. It is found that the distributions are a bit varied with different SBLs. It shows small repeated fluctuations with intervals almost equal to bin width. The fluctuations are more obvious, while the bin width is larger. Amplitude of fluctuation is reduced with smaller SBL bin width, meaning that a smaller SBL bin width brings smoother distribution of the faintest surface brightness. Consequently, reconstruction using a smaller SBL bin width can produce more realistic mock galaxies. We also check the impact of SBL bin widths on galaxy stellar mass and radius and find that the distributions are similar for different bin widths. In the following study, we reconstruct the galaxies with SBL bin width equal to 0.1.

3. Results

We use the angle in projection between the major axis of the central galaxy and the connecting line between the center of a satellite and host central to express the satellite spatial distribution. The central galaxy is defined as the most massive galaxy in each dark matter halo.

3.1. Satellite Alignment

For comparison with results of SDSS data at redshift $z \sim 0$, we further apply the SDSS selection limits, $m_r < 22.2$ mag, and dark matter halos mass lower limit in Y06, $M > 10^{12}\ h^{-1}\ M_{\odot}$, to obtain the comparative galaxy sample. We also divide the comparative galaxies into four subsamples, blue satellites, red satellites, blue centrals, and red centrals, to predict the galaxy alignment and compare with previous works. It is worth noting that the $M > 10^{12}\ h^{-1}\ M_{\odot}$ cut is applied for the purposes of comparison with the results in Y06 rather than accuracy (since it is noted in Section 1 that this cut might lead to incompleteness issues).

Figures 7 and 8 show the predicted alignment of satellite galaxies compared with previous studies. The galaxy sample is combined with those on three projected planes to increase the galaxy number and reduce the bias. θ ($0° \leqslant \theta \leqslant 90°$) is the angle on the projection plane between the direction of satellites relative to the central galaxy and the major axis of their host central. Satellite alignment strength is represented by the distribution probability function of θ, $P(\theta) = N(\theta)/\langle N_R(\theta)\rangle$, where $N(\theta)$ is the count of satellites in angular position bin θ, while $\langle N_R(\theta)\rangle$ is the average count of satellites in the same bin θ from 100 groups of random samples, in which we randomize the orientation of all central galaxies. The statistical error is Poisson error. This calculation is the same as that in Y06. We compare the alignment signal with previous works by the Kolmogorov–Smirnov (K-S) test. We randomly value the $P(\theta)$ within the error margin in each bin and repeat the K-S computation 100 times. The K-S probability is the average of K-S computations. The error is the standard deviation of average K-S probability. The distributions are more similar, while the K-S probability is much closer to 1 (K-S < 0.2 for two distinct distributions).

As shown in Figure 7, it is found that the probability function of our prediction roughly agrees with previous observation studies and theory work; however, our prediction of alignment signal looks slightly stronger than that in D14, utilizing the same simulation but with different galaxy identification. The K-S probability of drawing ours from the results of Y06 and D14 is 0.963 ± 0.0444 and 0.765 ± 0.0420, respectively. K-S$_{\rm Y-D}$ is 0.999 ± 0.0003. The interpretation is that our mock central galaxies have smaller radii and are located in the inner region of the host halo, where stellar components express a stronger alignment effect. This is in contrast to the prediction of Wang et al. (2014b), where host halos were used to shape central galaxies. We can find from the comparison between those three K-S tests in Figure 7 that the alignment in our study and that in D14 are both close to the observational result, but they are far from each other, for the significance levels. We check the cumulative distribution functions (CDFs) of those three alignments and find that the CDF in D14 is lower than that in Y06, while the CDF in ours is higher than that in Y06. It is implied that the alignment is weaker than our result but stronger than the result in D14. Those three alignments are the same, at significance levels.

We divide the comparative sample into different galaxy types to predict the galaxy alignment and compare with previous works, as shown in Figure 8. For red subsamples, our result is comparable to that of previous works. The K-S probabilities of red subsamples are all larger than 0.3.

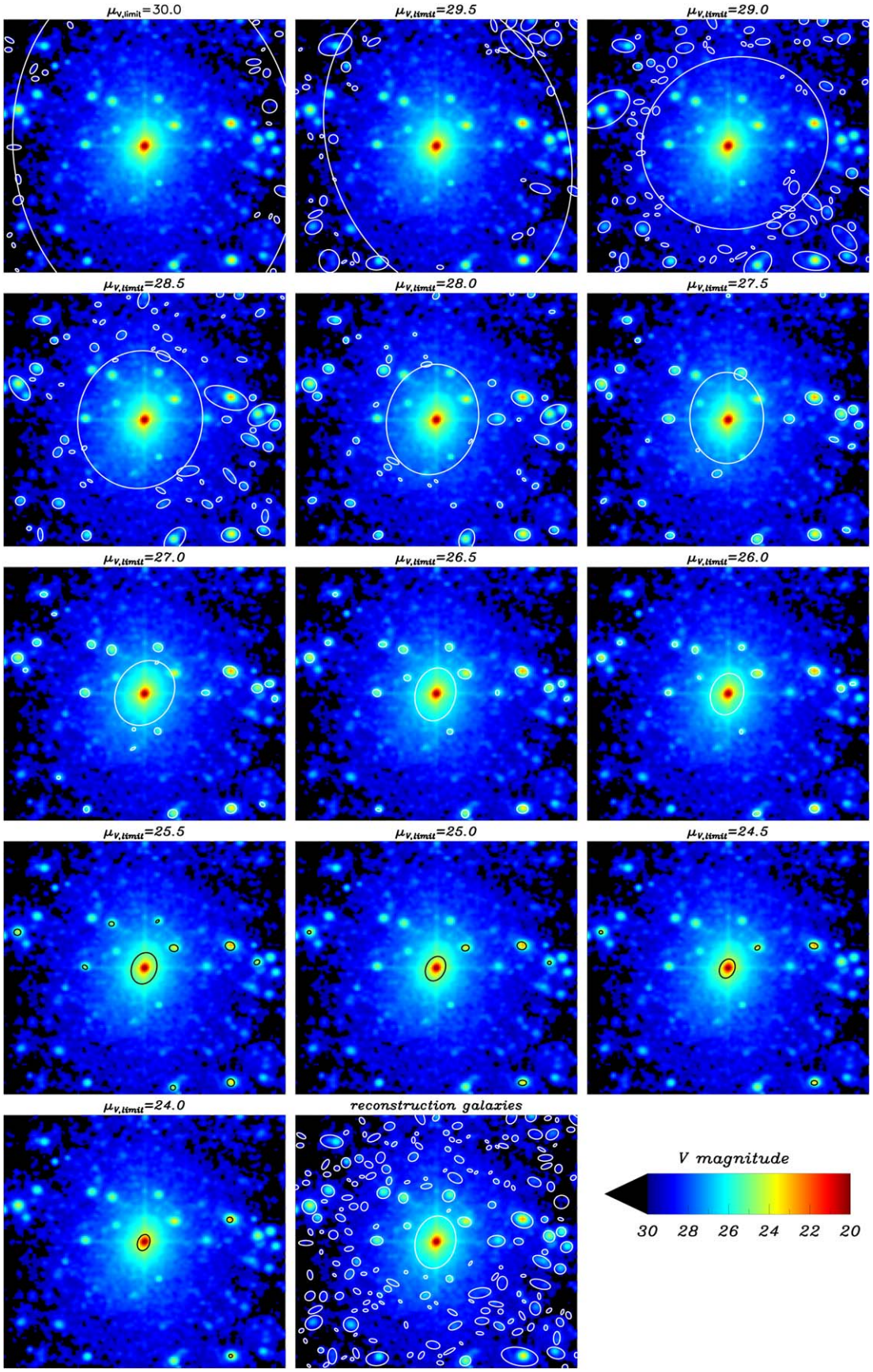

Figure 3. Galaxies defined by a series of SBLs with SBL width equal to 0.5 are illustrated. Applying the reconstruction procedure, the reconstructed galaxies are illustrated in the bottom right panel. The white (or black) solid lines are the ellipse fitting shape of galaxies. The unit of the horizontal and vertical axes is 4.5 h^{-1} kpc. Those galaxies are hosted in the most massive dark matter halo. We only plot the central region with 700 h^{-1} kpc × 700 h^{-1} kpc.

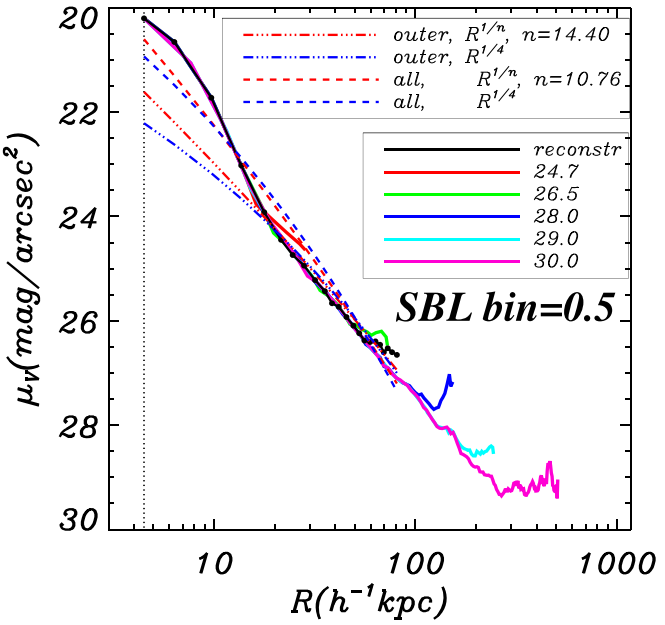

Figure 4. Reconstructed surface brightness profile with SBL bin width equal to 0.5 for the same galaxy in Figure 1 (black solid line). We do the $R^{1/4}$ or $R^{1/n}$ fitting as shown in the legend. For comparison with the galaxy in Figure 1, we plot the surface brightness profiles with four different SBLs as shown in Figure 1 (solid colored lines). The vertical dotted line represents the Plummer softening length in the simulation.

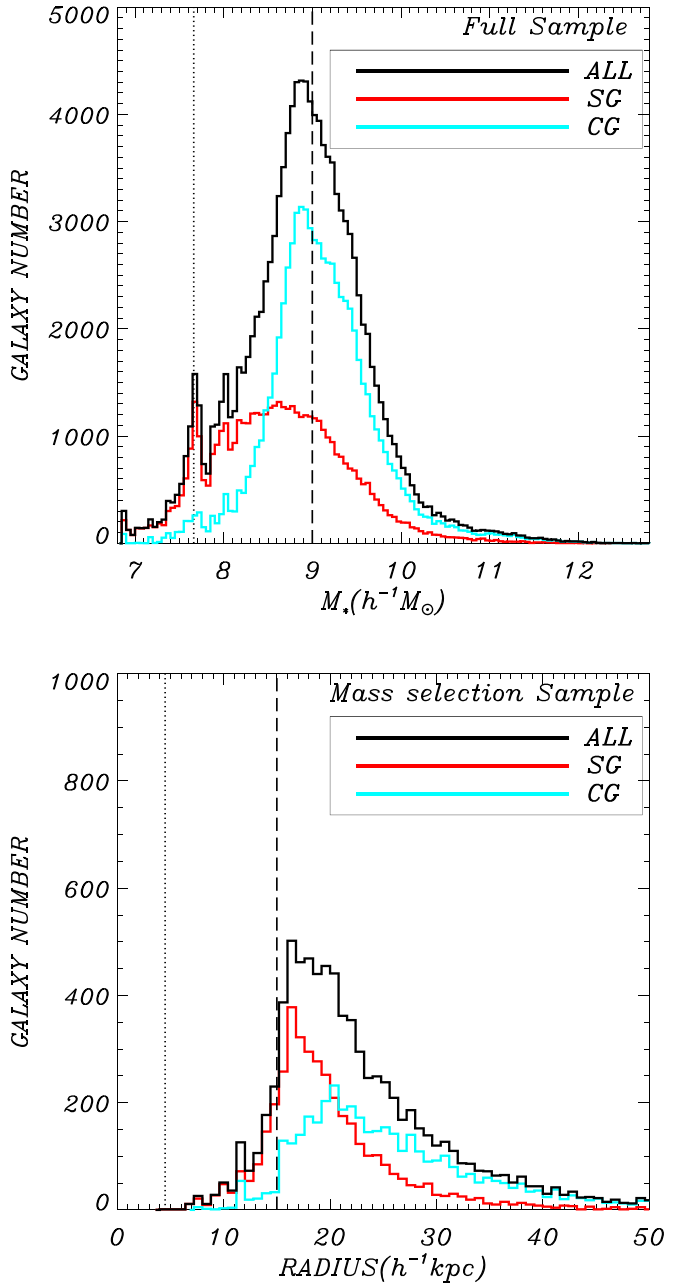

Figure 5. Top panel: stellar mass function of the different kinds of reconstructed galaxy samples with SBL bin width equal to 0.5, without any mass or size resolution criteria (i.e., full sample). Bottom panel: radius distribution of the different kinds of reconstructed galaxy samples with same SBL bin width (0.5), but including the galaxy mass resolution criterion $M_* > 9.2 \times 10^9\, h^{-1}\, M_\odot$ for centrals and $M_* > 4.6 \times 10^9\, h^{-1}\, M_\odot$ for satellites (i.e., mass selection sample) as discussion in Section 2.3. The cyan, red, and black solid lines mean satellite, central, and member (i.e., central + satellite) galaxy samples, respectively. The vertical dotted lines in those two panels represent the mass resolution and Plummer softening length in the simulation, respectively. The vertical long-dashed lines in those two panels represent $M_* = 10^9\, h^{-1}\, M_\odot$ and Radius $= 15\, h^{-1}$ kpc, respectively. All the plots are for the results in the $x - y$ plane.

Compared with results in D14, the difference is obvious for blue subsamples. For blue satellites, their number density in D14 increases with halo radius, contrary to the observation (e.g., Wang et al. 2014a). The vast majority of blue satellites in the inner halos are missing from the sample in D14 (as discussed in Section 3.2). Because blue centrals are often nonspherical and actively star-forming, their dynamics and alignment are more strongly influenced by feedback processes than for red centrals. When compared with the galaxy distribution in D14, we find that the misalignment of major axes of blue centrals between the inner region and outer region is larger than that of red centrals, which causes a larger difference for blue centrals than for the red subsample of galaxies. Because of the relatively small sample caused by the SDSS selection limits, the alignment signal of red centrals shows a larger scatter than others.

Compared with results in Y06, the alignment signals of our blue subsamples are much stronger. The prediction of alignment signals of the four subsamples looks similar to that in Kang et al. (2007, their Figure 3). However, because the simulation we used has a lack of AGN feedback, the centrals are too blue owing to overcooling. The color dependence needs further investigation. Finally, the difference between three kinds of K-S value in each panel of Figure 8 implies that the alignment signal of red galaxies in our study is closer to the result in observation. On the other hand, the blue galaxies in our study show much stronger alignment signals than observational results.

3.2. Satellite Radial Distribution

The left panel of Figure 9 plots the radial dependence of the average position angle of satellites. The distribution is in contrast to that of previous studies (e.g., Dong et al. 2014; Wang et al. 2018). We check radial distributions on three projected planes and find that there are similar distributions on three projected planes, but with big scatters. In the middle panel of Figure 9, it is found that the radial distributions of blue and red satellites are hugely different. In the inner region, blue satellites are more aligned with central galaxies than red satellites. And the dependence of red satellites on dark matter

Table 2
Sample Definitions

Full Sample	All Galaxies in the Simulation (Top Panel of Figure 5)
Mass selection sample	Galaxies with $M_{\rm cen,*} > 9.2 \times 10^9\,h^{-1}M_\odot$, $M_{\rm sat,*} > 4.6 \times 10^9\,h^{-1}M_\odot$ (bottom panel of Figure 5)
Fiducial sample	Galaxies with $M_{\rm cen,*} > 9.2 \times 10^9\,h^{-1}M_\odot$, $M_{\rm sat,*} > 4.6 \times 10^9\,h^{-1}M_\odot$ and Radius $> 18\,h^{-1}$ kpc (Figure 6)
Comparative sample	Galaxies with $M_{\rm cen,*} > 9.2 \times 10^9\,h^{-1}M_\odot$, $M_{\rm sat,*} > 4.6 \times 10^9\,h^{-1}M_\odot$, Radius $> 18\,h^{-1}$ kpc, $m_r < 22.2$ mag, and located in dark matter halos with $M > 10^{12}h^{-1}M_\odot$ (Figures 7 and 8)

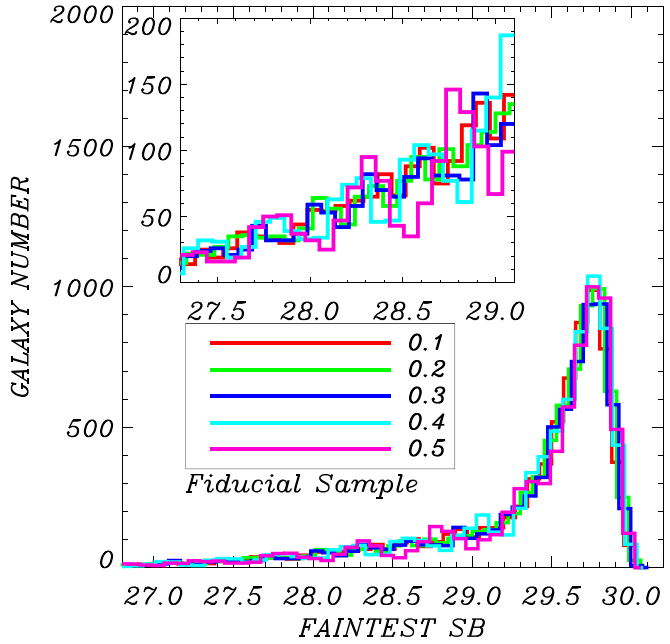

Figure 6. Dependence of fiducial galaxy number on the faintest surface brightness (faintest SB), i.e., the lowest value of surface brightness profile of galaxies, which is the mean surface brightness on the edge region of galaxies, with different SBL bin widths, [0.1, 0.2, 0.3, 0.4, 0.5], as shown by the legend. The fiducial sample is restricted by the mass and size resolution criteria as discussed in Section 2.3 ($M_{\rm cen,*} > 9.2 \times 10^9\,h^{-1}\,M_\odot$, $M_{\rm sat,*} > 4.6 \times 10^9\,h^{-1}\,M_\odot$, and Radius $> 18\,{\rm h}^{-1}$ kpc). All the plots are for the results in the $x - y$ plane.

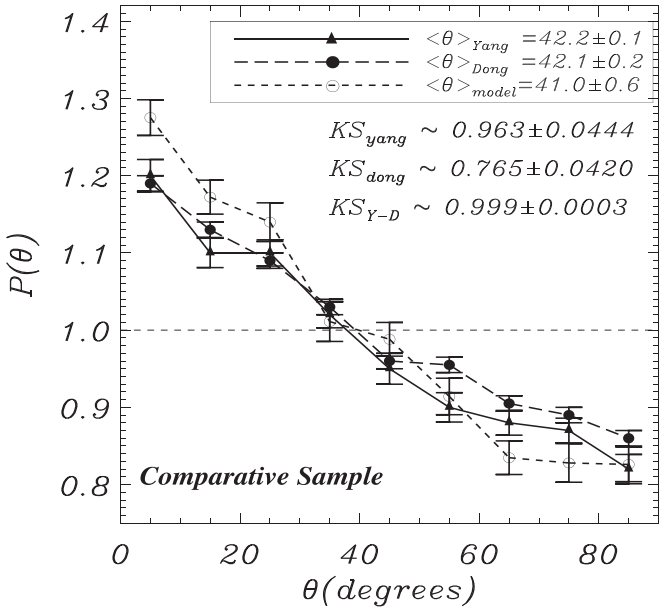

Figure 7. Predicted alignment of satellite galaxies at $z \sim 0$ of the comparative galaxy sample (short-dashed line with open circle), observational alignment (solid line with filled triangle), and previous theoretical prediction (long-dashed line with filled circle). The average angles $<\theta>$ are shown in the legends. We show the standard deviation of the average angles. The statistical error is Poisson error. K-$S_{\rm Yang}$ and K-$S_{\rm Dong}$ are the K-S probabilities of drawing our prediction from the results in Y06 and in D14, respectively. K-$S_{\rm Y-D}$ is the K-S probability between the results in Y06 and in D14. The galaxy sample is combined with those on three projected planes.

halo radius is opposite to that of blue galaxies, particularly in the outer region.

We check the galaxy radial number density profile and find that the number of red satellites is much larger than that of blue satellites, particularly in the inner halos. This density profile is more agreeable with the observational profile (Wang et al. 2014a) than that in D14, as shown in the right panel of Figure 9. Compared with the galaxy sample defined by the traditional substructure finder in D14, our sample includes more galaxies in the innermost region of dark matter halos. Those extra galaxies are close to their host centrals, while they are commonly treated as part of centrals by traditional substructure finders. As shown in the middle panel of Figure 9, the average distribution angle of inner galaxies ($<0.5R/R_{\rm vir}$) decreases with increasing radius. Lacking satellites in the inner region naturally causes the contrast of galaxy radial distribution between D14 and this work.

It has been proved that satellites' distribution is strongly dependent on galaxy properties (e.g., Yang et al. 2006; Brainerd & Yamamoto 2019) and the satellite alignment signal strongly correlates with satellite metallicity (e.g., Dong et al. 2014). We studied the color–metallicity–age relation and found that satellites with higher metallicity have bigger age, but for a given color, satellite age shows a huge distribution. This implies that the galaxy alignment dependence on metallicity is the reflection of age relation.

So as to discover the physical mechanism of satellites' radial distribution, we plot the dependence of age and metallicity of satellites on radius, as shown in Figure 10. The age and metallicity of galaxies are calculated by the average of age and metallicity of total components included by the galaxies. The age and metallicity in each bin of $\Delta(R/R_{\rm vir})$ are defined by the average age and metallicity of satellites located in the region from $R/R_{\rm vir}$ to $R/R_{\rm vir} + \Delta(R/R_{\rm vir})$. It is found that age and metallicity of satellites decrease with radius. Blue satellites are older and metal richer than red satellites within virial radii of dark matter halos. On the other hand, the age and metallicity deviation between the central and its satellites increases with larger radius. Compared with red satellites, blue satellites have their age and metallicity much closer to their central galaxies. It seems that blue satellites are a population close to centrals, but red satellites are galaxies accreted from nearby structure. The dependence of age and metallicity of satellites on radius in Figure 10 implies that satellites located in inner halos are older,

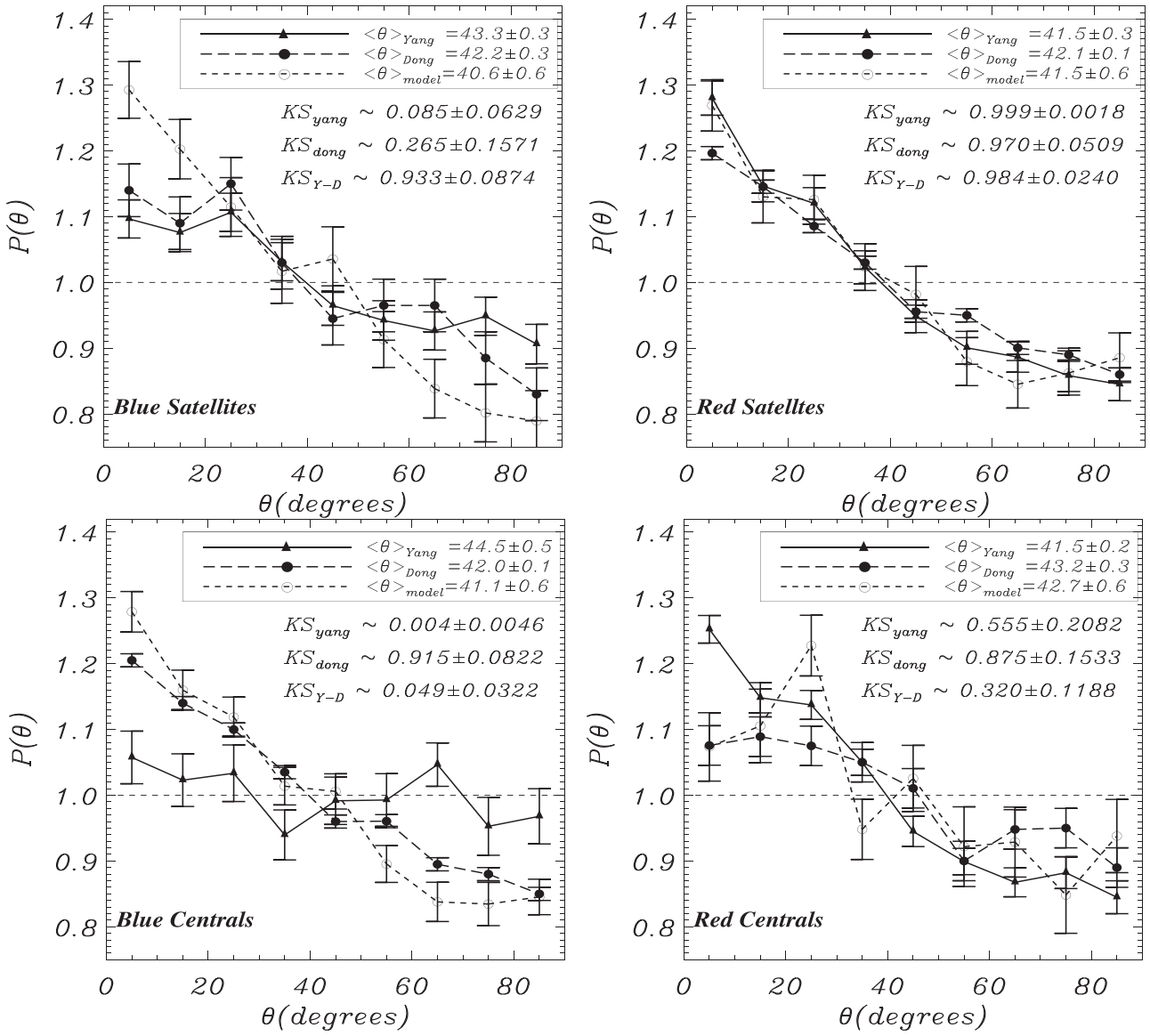

Figure 8. Predicted alignment of satellite galaxies at $z \sim 0$ of different types of galaxies as indicated by the text (short-dashed line with open circle), observational alignment (solid line with filled triangle), and previous theoretical prediction (long-dashed line with filled circle). The average angles $<\theta>$ are shown in the legends. We show the standard deviation of the average angles. The statistical error is Poisson error. K-S_{Yang} and K-S_{Dong} are the K-S probabilities of drawing our prediction from the results in Y06 and in D14 for each subsample, respectively. K-S_{Y-D} is the K-S probability between the results in Y06 and in D14. The galaxy sample is combined with those on three projected planes.

metal richer, and much closer to their host centrals than those located in outer halos.

The dependence of age and metallicity of satellites on halo radius illustrates that satellites located in inner halos and blue satellites are more likely formed at the same time as the central galaxy or early-merger remnants, while the distribution of those satellites seems to better trace the dark matter distribution (e.g., Jing & Suto 2002; Yang et al. 2006). On the other hand, satellites located in outer halos and red satellites are late-merger or accretion remnants, and their distributions are more asymmetrical (e.g., Wang et al. 2005).

3.3. Redshift Evolution

Figure 11 shows the dependence of satellites' spatial distribution on redshifts. The left panel shows the predicted alignment signals of satellites at five different redshifts $z \sim 0.0$, 0.5, 1.0, 1.5, and 2.0. In Table 3, we list the K-S probabilities of the predicted alignments drawn from an isotropic distribution. The K-S probability is bigger at high redshifts than that at low redshifts. Those results illustrate that satellites' distribution signal is stronger at lower redshifts. The middle panel represents that the average angle of satellite distribution is larger at a higher redshift. Those dependences of distributions on redshifts imply that satellites become more inhomogeneous with cluster evolution, which is consistent with the alignment signal in the MassiveBlack-II simulation (e.g., Bhowmick et al. 2020) and expected in Wang et al. (2010). There have been some results that are inconsistent with ours, for example, in Donoso et al. (2006), the alignment signal at z = 0.5 in SDSS DR4 is similar to the one in the local universe. However, their average distribution angle of satellites is 44°, which is a weaker alignment signal than that in Y06 (41°.3).

The right panel of Figure 11 shows the relation between radial distribution and redshift. The deviation of average angle

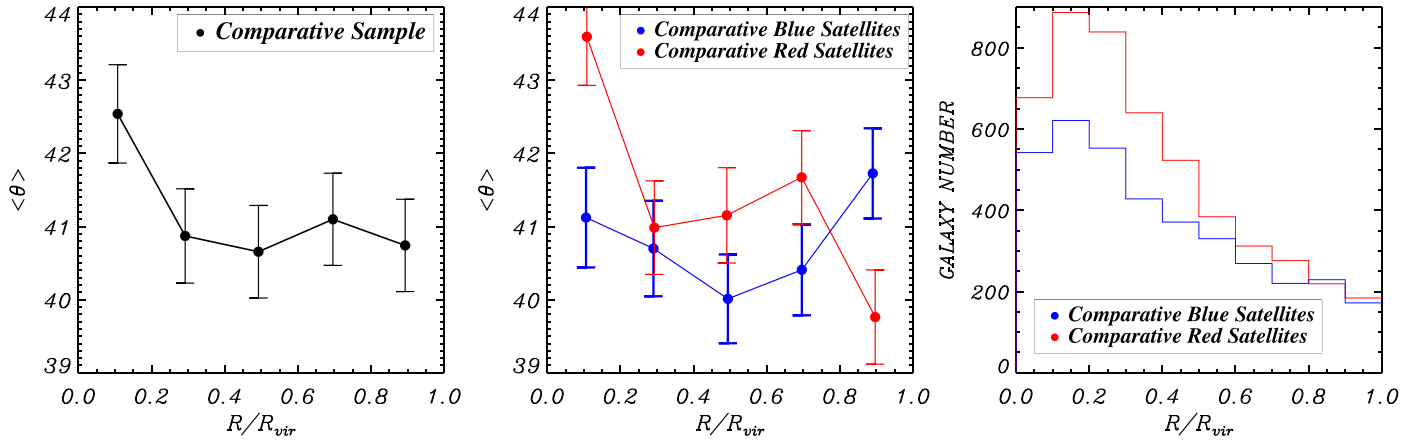

Figure 9. Dependence of average distribution angle on radius from the halo center normalized by halo viral radius at redshift $z \sim 0$. The galaxy sample is combined with those on three projected planes in the left panel. We divide galaxies into blue (blue line) and red satellite (red line) subsamples and plot the radial dependence in the middle panel and galaxy number density profile in the right panel. The error bar is the standard deviation of average angles of satellites in each radius bin.

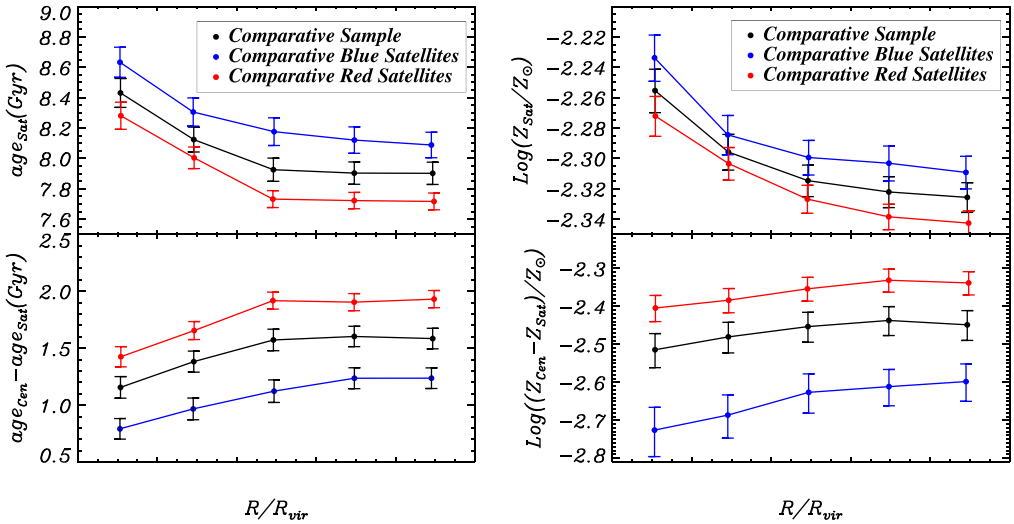

Figure 10. Dependence of satellite age and metallicity on radius. Top panel: radial distribution of satellites' age and metallicity. Bottom panel: radial distribution of deviation of age and metallicity between the central and its satellites. Black, red, and blue lines are results of full, red, and blue galaxy samples, respectively. The error bar is the standard deviation of average age and metallicity of satellites in each radius bin.

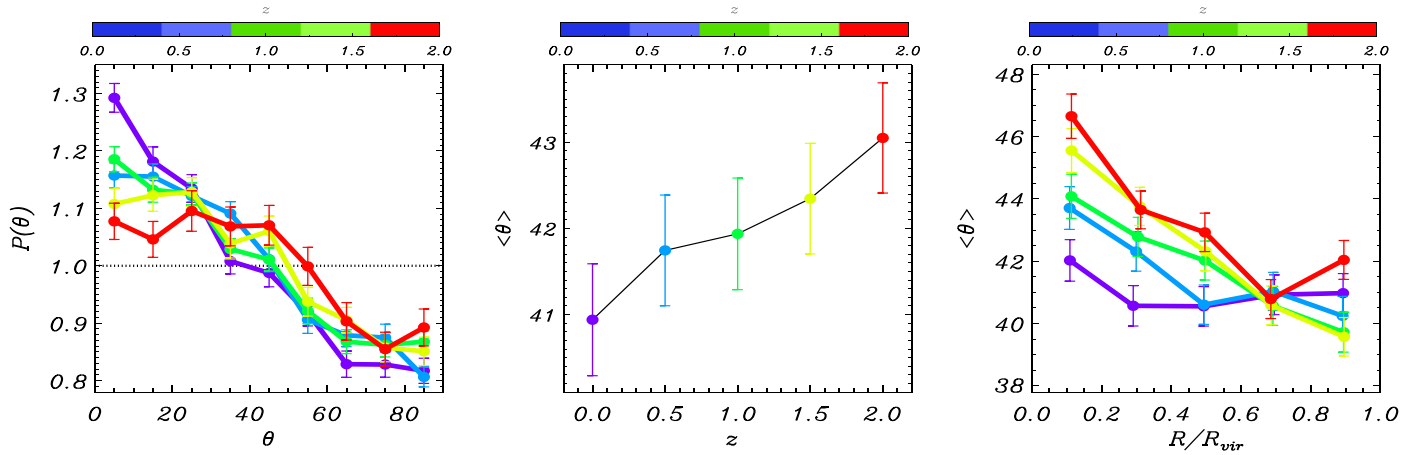

Figure 11. Left panel: predicted alignment signals of satellites at different redshifts. The statistical error is Poisson error. Middle panel: dependence of average distribution angle on redshift. Right panel: relation between average angle and radius of halos at different redshifts. The error bars in the middle and right panels are the standard deviation of average angles of satellites in each redshift and in each radius bin, respectively. The redshifts are $z = 0$, 0.5, 1.0, 1.5, and 2.0, as the color bar shows. The satellites are included by the fiducial samples.

Table 3
Kolmogorov–Smirnov Probabilities at Different Redshifts

Sample Redshift	K-S Probability
0.0	3.590×10^{-4}
0.5	1.290×10^{-3}
1.0	4.927×10^{-3}
1.5	2.949×10^{-2}
2.0	1.230×10^{-1}

Note. The probabilities are for the angular distribution of the satellites to be drawn from an isotropic distribution.

between the inner region and outer region increases with redshift. The average angle of satellites' spatial distribution in the inner region decreases, while that in the outer region increases, with cluster evolution.

The radial dependence of satellite distribution is getting weaker with time, but its original information is impressed in the dark matter halos and is not erased or reversed by the halo evolution. We test the evolution of radial distribution for blue and red subsamples. It is found that the radial distribution of blue satellites appears similar to that of red satellites at high redshifts ($z = 0.5, 1.0, 1.5, 2.0$) and differs only at larger radius with smaller average angle. In the inner part of the host halo, both red and blue satellites in the early universe show higher average distribution angles than those in the local universe. It is implied that the galaxies are far away from the direction of centrals' major axis owing to post-infall evolution, but this influence decreases with time.

4. Conclusions and Discussion

A wide variety of works have investigated the satellite spatial distribution. Current observations and theoretical results consistently agree that satellites are preferentially distributed along the major axes of host centrals, but slightly different in terms of intensity of alignment signal. Many kinds of theoretical study attempted to reduce the discrepancy with observations and achieved success on some degree.

In this paper, we explore the satellite distribution using an observational mimic galaxy definition, which differs from traditional substructure defined algorithms in hydrodynamical simulations. Our method is based on the projected observational surface brightness profile of each FoF group to define mock galaxies, with observational parameters. Using several surface brightness limits, a mock galaxy sample is reconstructed. This method avoids multiple galaxies connected together and a narrow galaxy region for the single surface brightness limit, as shown in Figures 1 and 4. In this way, the density profile of the galaxy is more consistent with that in observations, as shown in the right panel of Figure 9.

We study the alignment of satellites compared with previous predictions and the dependence of average angle of satellite distribution on viral radii of dark matter halos. We also study the redshift evolution of satellite distribution, which was rarely discussed in the literature. The results we obtained are summarized as follows:

1. The alignments of our reconstructed mock galaxies approximately agree with previous predictions. There are two discrepancies: (1) overall probability functions show slightly stronger alignment signals than those of previous predictions, and (2) the alignments of blue subsamples exhibit obviously stronger signals than observations.
2. Alignment strength of satellites is anticorrelated with the virial radii of dark matter halos in our work. It shows similar results for three projected images. We subsample the galaxy sample into red and blue galaxies and find that blue satellites are more aligned with major axes of centrals residing in the inner regions. And the radial distribution of satellites' age and metallicity decreases with radius. The age and metallicity of blue satellites are much closer to those of host centrals compared with red satellites.
3. The dependence of satellites' spatial distribution on redshifts is small but exists. Generally, the lower the redshift, the stronger the alignment signal, and the flatter the radial distribution curve. The strength of the alignment signal in our predictions is in broad agreement with observational results. More observation data are need to calculate satellite alignment signals at high redshifts.

In summary, compared with the traditional galaxy finder, our predicted satellite alignment is slightly stronger, particularly for blue subsamples. Defined galaxies (especially centrals) by the traditional galaxy finder include many outer components, and galaxy number density is underestimated in the inner region of dark matter halos (e.g., Klypin et al. 1999; Liu et al. 2010; Onions et al. 2012). We illustrate that our predicted probability functions of satellite distribution are still stronger than observational results. Considering a lack of AGN feedback in our simulation, we state that a complete galaxy formation model, e.g., including AGN feedback (e.g., Scannapieco et al. 2012; Cui et al. 2016; Sembolini et al. 2016), is important to reproduce the galaxy structure, or small-scale structure of the universe. Overall, satellite spatial distribution is dominated by red galaxies but sensitive to blue ones. Although our simulation cannot perfectly reproduce the satellite distribution, the comparison between prediction of simulations and observations is much fairer than that in previous studies. The difference between our predictions and the satellite alignment signal measured by Y06 is more reasonable than in previous studies owing to our reconstruction method, which has been designed to mimic the observations of ICL (Tang et al. 2018).

Our studies also imply that satellites are fallen into the halos from the direction of centrals' major axis, while the post-infall evolution has strong influence on the alignment signal. The post-infall influence decreases the strength of the alignment signal, causing the dependence of satellites' average angle on radii of host halos in our study. However, the decreasing influence of post-infall evolution is getting weaker for satellites with later infall times. The alignment signal of satellites is due to post-infall evolution and infall of galaxies along the nearby large-scale structure (LSS). This means that satellites are distributed more asymmetrically in the local universe.

Comparing the radial distribution, it is found that missing galaxies in the inner host halos in D14 is the main reason for the difference between the radial distributions in our study and in D14. The galaxy samples in Y06 and Wang et al. (2018) are obtained by a halo-based group finder (Yang et al. 2005), which is based on the FoF algorithm. We will apply our galaxy finder to SDSS data to study the difference between the galaxy sample in Illustris simulations (Vogelsberger et al. 2014) and

the sample in Y06 and Wang et al. (2018) in future work. Considering the incomplete galaxy formation model in our simulation code, we plan to reexamine the satellite radial distribution using results of Illustris simulations (Vogelsberger et al. 2014) and IllustrisTNG simulations (Pillepich et al. 2018, 2019), which include a much more complete galaxy formation model. The Illustris simulation has been used to analyze the satellite distribution by Brainerd & Yamamoto (2019), and it is shown that the median angle of three-dimensional satellites' radial distribution decreases with radius within the host dark matter halo.

In our studies, the dependence of satellite age and metallicity on halo radius can interpret the anticorrelation between alignment strength and halo radius. Satellites located in inner halos and blue satellites have more similar age to host centrals than satellites located in outer halos and red satellites, meaning that they are more likely concentrations by gravitational potential located at primordial density peaks within dark matter halos, according to the hierarchical clustering formation theory, or early-merger remnants. Therefore, the distribution of those kinds of satellites traces the dark matter distribution, which is strongly aligned in the inner part of host halos (e.g., Jing & Suto 2002; Kang et al. 2005a; Wang et al. 2014b). On the other hand, satellites located in outer halos and red satellites are more likely late asymmetrical merged or accretion remnants from the surrounding environment or LSS (e.g., Wang et al. 2005; Wang & Kang 2018).

Considering the dependence of alignment of satellites on LSS (e.g., Zhang et al. 2015; Wang et al. 2018), in the dense environments of LSS, the alignment signal of satellites is strengthened from Cluster (or Knot) to Filament, then to Sheet (or Wall), which is similar to our results that the alignment signal is reduced by the post-infall evolution. Because the angular momentum of matter in the Knot's environment is chaotic, the trajectory of satellite galaxies after falling is more likely to deviate from the direction of centrals' major axis (e.g., Zhang & Wang 2019).

The redshift evolution illustrates that the current galaxy distribution in dark matter halos is less homogeneous and more aligned with major axes of host centrals than the early universe. In other words, in the early universe, the galaxy distribution is almost symmetric. The evolution of galaxy distribution exhibits two kinds of galaxy dynamical history, implying two physical effects on galaxies, in the inner and outer halo region, respectively. With evolution, the outer galaxies are gradually located in a wider range caused by the halo gravitational potential. Meanwhile, the inner galaxies are distributed more preferentially aligned with the major axes of central galaxies influenced by the galaxy dynamical interaction and central astrophysical mechanism, which have a major impact on the evolution of small-scale cosmic structure (e.g., Springel et al. 2005; Mo et al. 2010). This scenario also explains why satellite distribution today is more inhomogeneous.

The authors thank the anonymous referee for useful suggestions. W.P.L. acknowledges support from the National Key Program for Science and Technology Research and Development (2017YFB0203300), the National Key Basic Research Program of China (No. 2015CB857001), and the NSFC grant (No.11473053). W.Y. acknowledge support by the NSFC projects (No. 11643005). The simulations were run in the Shanghai Supercomputer Center, and the data analysis was performed on the supercomputing platform of Shanghai Astronomical Observatory and School of Physics and Astronomy, Sun Yat-sen University.

ORCID iDs

Lin Tang (唐林) https://orcid.org/0000-0001-6395-2808
Yang Wang (汪洋) https://orcid.org/0000-0002-1512-5653

References

Agustsson, I., & Brainerd, T. G. 2010, ApJ, 709, 1321
Azzaro, M., Patiri, S. G., Prada, F., & Zentner, A. R. 2007, MNRAS, 376, L43
Bahcall, N. A., Ostriker, J. P., Perlmutter, S., & Steinhardt, P. J. 1999, Sci, 284, 1481
Bahl, H., & Baumgardt, H. 2014, MNRAS, 438, 2916
Bailin, J., Power, C., Norberg, P., Zaritsky, D., & Gibson, B. K. 2008, MNRAS, 390, 1133
Bertschinger, E. 1998, ARA&A, 36, 599
Bett, P., Eke, V., Frenk, C. S., et al. 2007, MNRAS, 376, 215
Bett, P., Eke, V., Frenk, C. S., Jenkins, A., & Okamoto, T. 2010, MNRAS, 404, 1137
Bhowmick, A. K., Chen, Y., Tenneti, A., et al. 2020, MNRAS, 491, 4116
Blanton, M. R., & Roweis, S. 2007, AJ, 133, 734
Blanton, M. R., Schlegel, D. J., Strauss, M. A., et al. 2005, AJ, 129, 2562
Boylan-Kolchin, M., Bullock, J. S., & Kaplinghat, M. 2011, MNRAS, 415, L40
Brainerd, T. G. 2005, ApJL, 628, L101
Brainerd, T. G., & Yamamoto, M. 2019, MNRAS, 489, 459
Bruzual, G., & Charlot, S. 2003, MNRAS, 344, 1000
Bullock, J. S., & Boylan-Kolchin, M. 2017, ARA&A, 55, 343
Cui, W., Power, C., Knebe, A., et al. 2016, MNRAS, 458, 4052
Davis, M., Efstathiou, G., Frenk, C. S., et al. 1985, ApJ, 292, 371
Dolag, K., Borgani, S., Schindler, S., Diaferio, A., & Bykov, A. M. 2008, SSRv, 134, 229
Dong, X. C., Lin, W. P., Kang, X., et al. 2014, ApJL, 791, L33
Donoso, E., O'Mill, A., & Lambas, D. G. 2006, MNRAS, 369, 479
Faltenbacher, A., Jing, Y. P., Li, C., et al. 2008, ApJ, 675, 146
Faltenbacher, A., Li, C., Mao, S., et al. 2007, ApJL, 662, L71
Feldmeier, J. J., Mihos, J. C., Morrison, H. L., Harding, P., & McBride, C. 2004, in IAU Symp. 217, Results from a Diffuse Intracluster Light Survey, ed. P.-A. Duc, J. Braine, & E. Brinks (San Francisco, CA: ASP), 86
Gonzalez, A. H., Zabludoff, A. I., & Zaritsky, D. 2005, ApJ, 618, 195
Holmberg, E. 1969, ArA, 5, 305
Jing, Y. P., & Suto, Y. 2002, ApJ, 574, 538
Kang, X., Jing, Y. P., Mo, H. J., & Börner, G. 2005a, ApJ, 631, 21
Kang, X., Mao, S., Gao, L., & Jing, Y. P. 2005b, A&A, 437, 383
Kang, X., van den Bosch, F. C., Yang, X., et al. 2007, MNRAS, 378, 1531
Klypin, A., Kravtsov, A. V., Valenzuela, O., & Prada, F. 1999, ApJ, 522, 82
Knebe, A., Gill, S. P. D., Gibson, B. K., et al. 2004, ApJ, 603, 7
Knebe, A., Knollmann, S. R., Muldrew, S. I., et al. 2011, MNRAS, 415, 2293
Kuhlen, M., Vogelsberger, M., & Angulo, R. 2012, PDU, 1, 50
Lin, W. P., Jing, Y. P., Mao, S., Gao, L., & McCarthy, I. G. 2006, ApJ, 651, 636
Liu, L., Yang, X., Mo, H. J., van den Bosch, F. C., & Springel, V. 2010, ApJ, 712, 734
Maller, A. H., & Bullock, J. S. 2004, MNRAS, 355, 694
Mo, H., van den Bosch, F. C., & White, S. 2010, Galaxy Formation and Evolution (Cambridge: Cambridge Univ. Press)
Onions, J., Knebe, A., Pearce, F. R., et al. 2012, MNRAS, 423, 1200
Pillepich, A., Nelson, D., Hernquist, L., et al. 2018, MNRAS, 475, 648
Pillepich, A., Nelson, D., Springel, V., et al. 2019, MNRAS, 490, 3196
Presotto, V., Girardi, M., Nonino, M., et al. 2014, A&A, 565, A126
Sales, L., & Lambas, D. G. 2004, MNRAS, 348, 1236
Sales, L. V., Navarro, J. F., Lambas, D. G., White, S. D. M., & Croton, D. J. 2007, MNRAS, 382, 1901
Samuroff, S., Mandelbaum, R., & di Matteo, T. 2020, MNRAS, 491, 5330
Sastry, G. N. 1968, PASP, 80, 252
Scannapieco, C., Wadepuhl, M., Parry, O. H., et al. 2012, MNRAS, 423, 1726
Sembolini, F., Elahi, P. J., Pearce, F. R., et al. 2016, MNRAS, 459, 2973
Springel, V. 2005, MNRAS, 364, 1105
Springel, V., & Hernquist, L. 2003, MNRAS, 339, 289
Springel, V., White, S. D. M., Jenkins, A., et al. 2005, Natur, 435, 629
Tang, L., Lin, W., Cui, W., et al. 2018, ApJ, 859, 85
van den Bosch, F. C., Aquino, D., Yang, X., et al. 2008, MNRAS, 387, 79

van den Bosch, F. C., & Ogiya, G. 2018, MNRAS, 475, 4066
van den Bosch, F. C., Ogiya, G., Hahn, O., & Burkert, A. 2018, MNRAS, 474, 3043
Vogelsberger, M., Genel, S., Springel, V., et al. 2014, MNRAS, 444, 1518
Walker, M. G., & Peñarrubia, J. 2011, ApJ, 742, 20
Wang, H. Y., Jing, Y. P., Mao, S., & Kang, X. 2005, MNRAS, 364, 424
Wang, P., & Kang, X. 2018, MNRAS, 473, 1562
Wang, P., Luo, Y., Kang, X., et al. 2018, ApJ, 859, 115
Wang, W., Sales, L. V., Henriques, B. M. B., & White, S. D. M. 2014a, MNRAS, 442, 1363
Wang, Y., Lin, W., Pearce, F. R., et al. 2015, ApJ, 801, 93
Wang, Y., Park, C., Hwang, H. S., et al. 2010, ApJ, 718, 762
Wang, Y. O., Lin, W. P., Kang, X., et al. 2014b, ApJ, 786, 8, (Paper I)
Weinmann, S. M., van den Bosch, F. C., Yang, X., et al. 2006, MNRAS, 366, 2
Yang, X., Mo, H. J., van den Bosch, F. C., & Jing, Y. P. 2005, MNRAS, 356, 1293
Yang, X., van den Bosch, F. C., Mo, H. J., et al. 2006, MNRAS, 369, 1293
Zhang, M.-G., & Wang, Y. 2019, RAA, 19, 181
Zhang, Y., Yang, X., Wang, H., et al. 2015, ApJ, 798, 17
Zibetti, S. 2008, in IAU Symp. 244, Dark Galaxies and Lost Baryons, ed. J. I. Davies & M. J. Disney (Cambridge: Cambridge Univ. Press), 176